# The effect of alloying elements on the ductility of Al-Mg-Si alloys

Magnus S. Remøe[a,d], Knut Marthinsen[a], Ida Westermann[a], Ketill Pedersen[b], Jostein Røyset[c] and Calin Marioara[b]

[a]Department of Materials Science and Engineering, Norwegian University of Science and Technology, NO-7491 Trondheim, Norway
[b]SINTEF Materials and Chemistry, NO-7465 Trondheim, Norway
[c]Hydro Aluminium RTD Sunndal, NO-6600 Sunndalsøra, Trondheim, Norway
[d]Contact e-mail: magnus.s.remoe@ntnu.no

**Abstract**

Experiments were conducted to document the combined effect of different alloying elements on the microstructure and associated stress-strain behavior of extruded Al-Mg-Si alloys, with a special emphasis on the ductility to fracture characteristics. Four alloys with different concentrations and relative amounts of Mg, Si, Fe, Cu, and Mn were selected for examination. In order to obtain an accurate description of the strength-ductility relationship, tensile testing was performed with a laser extensometer, and scanning (SEM) and transmission microscope (TEM) studies were carried out to correlate the microstructure and fracture characteristics with the stress-strain behavior. Excess-Si (Mg/Si<1.73) was found to have a detrimental effect on the ductility of Al-Mg-Si alloys without the presence of additional alloying elements, leading to fracture occurring partly intergranularly. This was linked to the segregation of free Si at grain boundaries, forming coarse Si-particles, and the formation of $Mg_2Si$ particles during solution heat treatment. Adding Fe and Cu improved the ductility and strength, which could be attributed to a lower solvus temperature and increased formation of primary particles, resulting in less free Si for embrittlement of grain boundaries. The highest ductility was found by introducing Mn, which in addition to tie up free Si to second-phase particles, suppressed recrystallization by forming dispersoids. The most desirable combination of tensile strength and ductility was found in an excess-Mg alloy (Mg/Si>1.73) with additions of both Mn and Cu.

*Keywords:* Extrusion, Al-Mg-Si, laser extensometer, electron microscopy, ductility, excess-Si

## 1. Introduction

Aluminum and its alloys have been known and utilized for over a century, but are still regarded as materials with valuable potential for the future. Their attractive properties in terms of e.g. specific strength and corrosion resistance combined with an excellent potential for recycling, make them appealing for numerous applications. Age hardenable Al-Mg-Si alloys are among the most widely used aluminium alloys due to their beneficial combination of cost and properties, and in recent years efforts have been made to further improve their final properties through alloying and process optimization, in order to make them attractive for new applications, e.g. sheets for car body panels in the automotive industry and extrusion alloys as load-bearing components for structural applications. For most of these applications an optimum combination of strength and ductility is required.

Ductility is generally defined as the amount of deformation a material can withstand prior to fracture. Combined with strength, it is also a measure of how much energy the material can absorb in e.g. a collision, and is therefore highly relevant for automotive
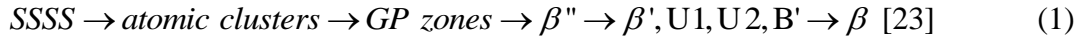
1

applications. To increase strength, alloying elements are commonly introduced as they influence the dislocation generation and mobility through solid solution strengthening and solute drag, the formation of hardening precipitates and/or the recrystallization behavior [1-5]. These strengthening mechanisms affect the ductility in different ways, but ductility is generally found to decrease with increasing strength [6, 7]. Lloyd [6] reported that the fracture strain for aluminium alloys with fairly similar microstructures seems to have an inverse linear relationship with the yield strength.

As the material is plastically deformed, work hardening occurs as the dislocation density increases through the interaction of dislocations with solute atoms, other dislocations and non-shearable precipitates [8]. The tensile strain, or elongation prior to necking, is highly dependent on the work hardening and strain rate sensitivity of the material, and is usually found to increase with higher work hardening rates [9, 10]. With sufficient deformation of a ductile alloy, dislocations tend to pile up at sites which impede their migration. A high level of localized stress is therefore associated with these regions, which may result in the formation of small cracks or voids [11, 12]. As stress intensities increase, these microvoids grow, and eventually coalesce to form the well-known dimpled fracture surface for ductile materials. Primary particles consisting of mainly Fe, Mn, and Si are typical sites for nucleation of such microvoids, either by their cracking or by decohesion of particle and matrix interfaces [11, 13]. These particles have a slight effect on necking, but a significant effect on fracture characteristics.

Primary particles normally contain Fe, which is traditionally an unwanted element in aluminum, but is mainly always present due to the difficulty of removing it completely from the molten metal. Fe has an almost negligible solubility in the aluminum matrix (~0.04 wt% at 928 K (655 $^{\circ}$C) [14]), and mainly participates in the formation of non-soluble particles during solidification. These particles do not dissolve, but they may transform into other phases. During homogenization, both cubic α-AlFeSi, and β-AlFeSi may be present after solidification of Al-Mg-Si alloys. Body centered cubic (bcc) α-AlFeSi has been found to have a composition close to $Al_{12}Fe_3Si$ (e.g. [14]), while the simple cubic α-AlFeSi has a composition close to $Al_{13}Fe_3Si_{1.5}$. The β-particle is assumed to be $Al_5FeSi$. The latter is known to result in poor ductility and formability [15, 16]. During homogenisation, a transformation from β- to α-particles occurs, and the transformation is accelerated with increasing homogenisation temperatures [17]. At the same time, the transformation process involves a transfer of Si from β to the matrix, leaving more Si for ageing precipitation [18]. The conditions for primary particle formation in Al-Mg-Si alloys have been shown to change with the introduction of Mn, leading to the formation of $Al_9Mn_3Si$ [19], and easing the transformation from β- to α-particles during homogenization [20].

Another important role of transition metals such as manganese is to form dispersoids during homogenization. Due to their slow diffusivity in the aluminum matrix, these particles are usually smaller than 0.5 μm. Dispersoids are known to delay or hinder recrystallization during thermomechanical processing, which may be beneficial for theproperties by retaining the deformation substructure, through the pinning of subgrains [21]. Dispersoids have also been found to increase work hardening as they cause the introduction of geometrically necessary dislocations surrounding them [13, 22]. However, Mn may also remain in solid solution after homogenisation and extrusion, and affect the work hardening through solid solution hardening. The effect of solute atoms on the work hardening behavior varies with the alloying element in question. Ryen et al. [4] found an almost linear concentration-strength relationship for Mg in solid solution, at a given strain. This was also found for Mn, but with a much larger strength contribution in the initial stages. Fe and Mn in solid solution have been found to give a significant contribution to the work hardening of aluminium alloys even at very low concentrations [4, 5].

In Al-Mg-Si alloys without additional alloying elements, the ageing precipitation sequence is currently known to follow the development described below, with the precipitated particles mainly following different compositions of the formula $Mg_xSi_y$:
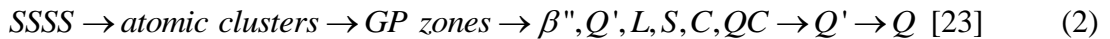
$$SSSS \rightarrow atomic\ clusters \rightarrow GP\ zones \rightarrow \beta'' \rightarrow \beta', U1, U2, B' \rightarrow \beta \quad [23] \quad (1)$$

The GP-zones and β'' phases are partially coherent, with a needle shape. The strengthening effect is thought to be strongest for β'' ($Mg_5Si_6$ [24]), which is therefore the most commonly observed precipitate at the peak aged condition, temper T6.

Studies have shown that the presence of excess-Si may result in a modification of the composition of the metastable phases, especially in the early stages of precipitation [25, 26]. Moreover, the reduction in Mg:Si ratio in zones and clusters in excess-Si alloys has been found to lead to increased precipitation and strengthening [25, 28], and these alloys are therefore often found in automotive applications, due to the necessity of fast ageing response in the paint bake cycle [25, 29].

If the material displays significant weaknesses at the grain boundaries, the fracture mode may not be completely ductile. Such weaknesses are most commonly related to the precipitate free zone (PFZ) and/or coarse grain boundary particles. Intergranular fracture may thus occur prior to complete fracture by void coalescence. Such events have been shown to reduce the ductility of Al-Mg-Si alloys containing excess-Si. Aucote and Evans [28] found that a significant amount of excess Si participated in the formation of pure Si particles at grain boundaries, increasing the fraction of facets corresponding to intergranular fracture. Even though Fe may reduce ductility by cracking of primary particles or void formation adjacent to them, it was suggested by Kato et al. [30] that the introduction of Fe may reduce the risk of intergranular fracture of excess-Si alloys, and in that way improve ductility. This was partly associated with a reduction in grain sizes due to the effect of particle stimulated nucleation (PSN) during recrystallization, resulting in an improved ductility for a given strength level. However, it was also suggested that Fe interacts with free Si in some way, to reduce segregation of the latter to grain boundaries.

It is well known that the presence of Cu significantly changes the precipitation behavior. The precipitation sequence in alloys with additions of Cu is currently found to be:

$$SSSS \rightarrow atomic\ clusters \rightarrow GP\ zones \rightarrow \beta'', Q', L, S, C, QC \rightarrow Q' \rightarrow Q \quad [23] \quad (2)$$

The chemical composition of both Q' and Q is expected to be $Al_4Cu_2Mg_8Si_7$ [21] while the precursory phases have a composition close to this, and are mostly Cu-containing and disordered with an Mg:Si ratio close to 1 [23, 31]. Marioara et al. [23] found that in an excess-Si alloy containing 0.3 wt% Cu, the β''-precipitates observed at peak strength only amounted to 20-30% of the total amount of particles. The remaining precipitates had needle or plate morphologies and consisted of Cu-containing GP zones and precursory phases for Q'. These precursory phases are known to give a significant strengthening effect to Cu-containing Al-Mg-Si alloys at peak strength, especially the lath or needle shaped L phase [23, 32]. In addition to increasing strength, Kato et al. [30] reported a significant increase in ductility with increasing Cu-content for excess-Si alloys. This was suggested to be due to an improved coherency between the grain boundary precipitates and the aluminum matrix.

The main objective of this study has been to provide new data, and a more comprehensive understanding of how the above-mentioned alloying elements influence the microstructure, and consequently affect the strength and ductility of selected Al-Mg-Si alloys. The present work was triggered by promising results into the effects of Fe and Cu on ductility, reported by Kato et al. [30].. However, the causes of their results werenot thoroughly documented in their paper, anda more in-depth understanding of the microstructural

manifestation and deformation behavior was required. Tensile testing was performed to examine the latter, and a state of the art laser extensometer was used as conventional extensometers are unable to accurately measure the stress-strain behavior after necking. The microstructural features were investigated by various techniques in scanning (SEM) and transmission (TEM) electron microscopy, e.g. electron backscatter diffraction (EBSD), energy-dispersive X-ray spectometry (EDS) and backscatter electron imaging (BSE).

There is a strong push in the industry for high strength Al-Mg-Si alloys with improved combinations of strength and ductility. So far, a lot of work has been focused on the precipitation behavior and related strength behavior of Al-Mg-Si alloys [23, 25, 27, 29], however, much less attention has been given to the ductility and fracture behavior. The current study therefore provides a necessary contribution to this topic.


## 2. Experimental

### 2.1. Materials

A flow chart of the experimental procedure is presentedin Figure 2. Four alloys, with chemical composition as shown in Table 1 were direct chill (DC)-cast at Hydro Sunndalsøra, and homogenised for 2 hours and 15 minutes. The homogenisation heat treatment was carried out at 848 K (575 $^{o}$C) for all alloys except Ref, which was homogenised at 833 K (560 $^{o}$C). The heating rate was set to 4.6 K/min until reaching 773 K (500 $^{o}$C), and subsequently 1.0 K/min until reaching the final temperature. The cooling rate from homogenisation was 9.4 K/min. In order to avoid local melting, the billets were preheated to approximately 823 K (550 $^{o}$C), and subsequently cooled down to 773 K (500 $^{o}$C) prior to extrusion. They were then extruded to round bars of 20 mm diameter in an 800 tons laboratory press. The extrudates were water-quenched continuously as they exited the die.

The reference alloy, denoted Ref, and alloys A and B, contained a similar amount of Si (~1 wt%) and Mg (0.65-0.8 wt%), which is reflected by their Mg:Si ratio. Alloy C on the other hand contained only 0.52 wt% Si, while the Mg-content in turn was higher relative to the other alloys, resulting in an Mg:Si ratio corresponding to an excess Mg alloy. As compared to the reference alloy, 0.8 wt% Cu was added to alloy A, and the Fe content was increased to 0.5 wt%. Only Mn was added to alloy B, at 0.55 wt%. The same amount of Mn was added to alloy C, but this alloy also contained 0.4 wt% Cu. Alloy D was added as a supplementary alloy, to isolate the effect of Fe, and has the same composition as alloy A, bar the Cu. Only alloys Ref, A, B and C were investigated fully; alloy D was only included in the tensile tests.

### 2.2. Hardness testing

Hardness tests were conducted according to the Vickers standard to determine the ageing time necessary to reach peak hardness in each alloy. Slices of approximately 1 cm thickness were cut off the extrusion bars in a Struers' Discotom-5 and thereafter solution heat treated in a salt bath at 803 K (530 $^{o}$C) for 10 minutes, before being water quenched. After natural ageing for 4 hours in room temperature, they were artificially aged in an oil bath at 443 K (170 $^{o}$C) for 5, 20, 60, 150, 360, 900, 2100 and 4500 minutes. After ageing, the samples were immediately water quenched, and ground with Struers grinding papers down to a grain size of 15 µm. Five indentations per condition were carried out in a Matsuzawa DVK-1S with 1kp load, and the average Vickers Pyramid Number (HV) was used to plot the hardness curves.

### 2.3. Scanning electron microscopy (SEM)

To achieve an optimal understanding of the behavior and microstructure in the extrusion direction, microscopic studies in SEM were carried out in the RD-ED plane, corresponding to the radial (RD) and extrusion direction (ED), respectively.

The samples for investigation of the primary particle distribution in SEM were solution heat treated in a salt bath at 803 K (530 $^o$C) for 10 min, water quenched, and cold mounted in Struers Clarocit solution. Thereafter, they were ground in the same manner as the samples for the hardness tests, and polished with a fabric with diamond spray of grain sizes down to 1 μm. The samples for the other investigations and operation modes in SEM were prepared similarly, with additional steps described below.

For the chemical analysis (EDS) of primary particles, an additional polishing step was applied to the samples. They were chemically polished with an active oxide polishing solution (OP-S) for 2 minutes, to separate the particles from the matrix and thus ensure superior signals with less noise from the surroundings. The phases of 8 primary particles in each alloy were identified by comparing the relative amount of Fe/Mn and Si found in the analyses. Due to some likely interaction between the penetration volume and the matrix, the aluminium peaks were disregarded. Polishing with OP-S was also used to reveal the grains when investigating possible Si particles on the grain boundaries, but only for 10 seconds, and followed by polishing with water for 4 minutes.

For EBSD (electron backscatter diffraction) investigations, samples of aluminum require electro-polishing to attain satisfactory indexing results. This was done in a Struers Lectropol-5, using an A2 electrolyte kept at 248 K (-25$^o$C). This method was used to more accurately determine the grain size by employing the EDAX/TSL OIM software. The grain tolerance angle was set to 5$^o$, and the minimum grain size to 1 μm.

Various investigations and operation modes in SEM require different settings to obtain optimal results. The settings applied in the Zeiss Ultra 55 LE SEM used in the present work, are specified in Table 2.

The images for the particle analysis required further treatment by an image processing software. The freeware ImageJ [34] was employed to find averages of the particle characteristics in three images for each alloy. To achieve an intuitive representation of the particle size, the area of each particle was converted to the Equivalent Circle Diameter (ECD). To obtain an impression of the particle shapes, the maximum and minimum feret diameters were calculated, which refer to the longest and shortest distance between any two points in a given particle, respectively. The ratio of the two feret diameters was calculated for each particle.

*2.4. Transmission electron microscopy (TEM)*

To achieve adequately thin samples for precipitate studies at 200 kV in Jeol JEM-2010 (TEM), slices of the extrusion bars were cut as thin as possible, and ground down to ~0.1 mm thickness. Small discs of 3 mm diameter were subsequently removed from the polished slices, and electropolished in a Struers Tenupol-5 with an electrolyte consisting of 1/3 $HNO_3$ and 2/3 methanol. The electrolyte was cooled down to 248 K (-25$^o$C), and the voltage was set to 20 V.

*2.5. Tensile testing*

Tensile testing was performed according to standard NS-EN ISO 6892-1. Three parallels of each alloy were prepared as round standard tensile specimens of 40 mm gauge length, with a cross-sectional area of 6 mm diameter. These were aged according to the findings from the hardness tests, to induce the peak hardness condition, T6. As conventional tensile tests only offer reliable information until the point of necking, a laser extensometer was employed to evaluate the ductility until the point of fracture. The laser extensometer was used with the instrument Instron 100 kN at a nominal strain rate of 1.2 mm/min. The laser

extensometer measures the decrease in cross-sectional area, or more precisely the projected diameter, during testing. The neck is here assumed to be elliptical [13], and thus two perpendicular lasers measures the decrease in diameter ($D$) at two places, providing the original cross-sectional area, $A_0 = \frac{\pi}{4} D_0^2$, and the instantaneous area, $A = \frac{\pi}{4} D_1 D_2$. The average strain at a given point may then be calculated as

$$\left( \varepsilon_x \right)_{avg} = \ln \left( \frac{A_0}{A} \right) \tag{3}$$

During tensile testing a triaxial stress state is introduced after neck initiation, resulting in a higher registered stress in the neck than what would actually be present if uniaxial stress conditions still prevailed. An expression keeping this new stress state in mind is provided by the Bridgman analysis [35], and is used to obtain a more precise representation of the actual stress conditions. The approximate uniaxial stress has been calculated through the following Bridgman equation:

$$\sigma = \frac{(\sigma_x)_{avg}}{(1 + 2R/a)[\ln(1 + a/2R]} \tag{4}$$

where $\sigma$ is the corrected stress, $(\sigma_x)_{avg}$ is the measured stress in the axial direction, $R$ is the curvature and $a$ is the radius of the neck [36]. Due to the relative difficulty with which one is able to measure the curvature of the neck, an approximation to the ratio of $a/R$ has been modelled. Le Roy et al. [37] proposed the following relationship

$$\frac{a}{R} = 1.1(\varepsilon_p - \varepsilon_u) \tag{5}$$

where $\varepsilon_p$ is the plastic strain at a given point after necking, and $\varepsilon_u$ the strain at the point of neck initiation.

## 3. Results

### 3.1. Grain structure
EBSD maps in Figure 2 reveal a completely recrystallized microstructure for alloys Ref and A after extrusion and solution heat treatment. The maps of the Mn-containing alloys display a somewhat mixed grain structure (note that only high angle grain boundaries are shown (misorientation angle >15°). Still mainly a non-recrystallized (fibrous) grain structure prevails, as shown in the (100) pole figures, which reveal a sharp deformation texture for these alloys. The smaller grains along the grain boundaries of the original grains are likely an effect of a certain amount of extended recovery or dynamic recrystallization.

The grain size distributions of the recrystallized alloys are shown in Figure 3, and reveal that the distribution is slightly shifted towards smaller grain sizes for alloy Ref, as compared to A. This is also reflected by the fitting parameter $b$ of the distribution fitting exponential decline ($f = y_0 + a exp(-bx)$), being higher for Ref, and indicating a sharper slope. Their average grain sizes were estimated to be 75.6 ± 57.6 and 92.0 ± 67.8 μm, respectively, with the large standard deviation indicating an inhomogeneous microstructure. The (001) pole figures show a very weak texture for these two alloys.

The grain size distributions for alloys B and C have not been included, as a size distribtution of grains in these cases, only based on high angle grain boundaries, would not be representative for the grain structure of these alloys, as the structure mainly consist of subgrains with lower misorientations not displayed in Figure 3c and d.

## 3.2. Primary particle sizes and spatial distribution

Visual inspection of the SEM images from the particle distribution analysis reveals that all alloys contain elongated primary particles. Figure 4 shows an example of the SEM images, taken from the reference alloy. The particles are inhomogenously dispersed, with the particles aligned along stringers in the extrusion direction. The analyses were taken as an average from three different images of every alloy, each covering an area of 1.48 mm$^2$.

Figure 5 shows that the size distribution of particles in B and C is shifted towards smaller particles as compared to those for alloys Ref and A. This is indicated by the parameter $X_0$ of the log normal distribution fitting ($f = aexp(-0.5(ln(x/X_0)/b)^2)/2)$, which represents the mean particle sizes. Parameter $b$ represents the distribution spread, and is similar for all alloys, but slighly larger for alloy B. Primary particles larger than 6 µm are observed in all alloys except alloy C, where the largest particles have an ECD of 4.5 µm. The feret diameter ratio is larger for alloys B and C, especially for particles smaller than 4 µm, indicating rounder particles. The large error bars for large particles are a consequence of few particles found in this size range.

Table 3 shows that more than twice as many primary particles were found in alloy A, as compared to the reference alloy. The particles in alloy A were also found to be slightly larger in average, and consequently covering a significantly larger area. In comparison, the Mn-containing alloys contained smaller particles, with a higher number count than the reference alloy. A higher count, and smaller particles, was found in alloy C as compared to alloy B. Note that the average ECD is different than $X_0$ for the distribution fittings. This is due to the distribution fittings being based on the bin counts, while the ECD values in the tables is the average of every particle counted in each alloy.

The chemical composition of the particles was investigated by EDS, and the results are shown in Figure 6, where the linear curves represent the compositions of the expected primary particle phases. Due to interaction with the aluminium matrix, the phase compositions have been extrapolated, and although the phases cannot be identified uniquely by EDS, such a procedure gives a fair indication [38]. The plot suggests that most of the primary particles analyzed in alloys Ref and A belong to the β-AlFeSi phase, and simulations by the solidification and homogenization microstructure model Alstruc [39, 40] were found to agree with this result. The particles in alloys B and C all contained a significant amount of both Mn and Fe, and aligned along the $Al_{13}(Fe,Mn)_3Si_{1.5}$-line. These results are also consistent with simulations by Alstruc [39, 40], which suggested that all particles in alloys B and C are likely of the α type.

## 3.3. Ageing behavior

According to the ageing curves in Figure 7, alloy A and C displayed the highest peak hardness values, with 143 ± 1.8 HV1 and 130 ± 2.3 HV1, respectively. The other two alloys peaked just below 120 HV1. Based on the findings from the hardness tests, the ageing times to peak hardness were chosen to be 35 hours at 443 K (170 $^o$C) for alloy A, and 15 hours for the other three alloys. The ageing curves may be divided in two stages in relation to the behavior before and after 1 hour. A rapid increase in hardness for the Cu-containing alloys (A and C) was observed in the initial stages, while no significant increase was observed in the first hour in the two excess-Si alloys without Cu (Ref and B). The relation is reversed after 1 hour, where the curve for alloy C flattens, with only a limited increase in hardness until the peak condition is reached. In this stage, the excess-Si alloys display the largest age hardening rate, including the Cu-containing excess-Si alloy A.

## 3.4. Stress-strain behavior

Results from the tensile tests are shown in Table 4 and Figure 8. The black lines in Figure 8 show the non-corrected curves, and the coloured lines indicate the Bridgman correction. The excess-Si reference alloy went to fracture at the lowest strain, with 23.1% elongation, and also showed the lowest tensile strength with 358 MPa. In comparison, the addition of Fe and Cu resulted in both a significantly higher tensile strength and ductility for alloy A, with 434 MPa and 42.9% elongation. The ductility also significantly improvedwith the addition of Mn, with alloy B showing the largest elongation to fracture, corresponding to 79.2%. Alloy C showed the best combination of properties, and elongated to 64.6% prior to fracture while also displaying the highest tensile strength, with 465 MPa. Alloy D (similar alloying content as A, but without Cu) had a slightly lower strength than the reference alloy, and a somewhat larger elongation to fracture.

### 3.5. Fracture surfaces

SEM images of the fracture surfaces of the tensile specimens in Figure 9 reveal only a slight decrease in fracture surface cross-sectional area for the reference alloy, while for alloy A it is more pronounced. The two fibrous alloys displayed an even larger decrease in cross-sectional area, corresponding to their superior ductility. These two alloys also exhibit a spiral shape in the fracture surface. All fracture surfaces have a circular cross section, indicating that the assumption of an elliptical cross-section during straining is valid for these specimens.

Figure 10 shows the fracture surfaces at higher magnification. Both recrystallized alloys give clear indications of intergranular fracture, although there is a notable difference in dimple fraction between alloys Ref and A. The more ductile Cu-containing alloy A has fewer facets, while these are more prominent in the reference alloy. No facets were found on the fracture surfaces of alloys B and C. Increasing the magnification further, elongated primary particles were easily observed inside the dimples of all alloys.

### 3.6. Grain boundary particles

The grain boundaries were examined in SEM, and several dark particles were found in the reference alloy (indicated with arrows in Figure 11a). These were analysed by EDS, and the results are shown in Figure 11b. The particles either contained both Mg and Si, or were found to consist only of Si, and were mostly in the size range 0.5-1 μm. Similar particles were found on the grain boundaries in alloy A, but much fewer. In the Mn-containing alloys (B and C), the EDS analysis in SEM revealed particles containing Mn and Si, but these were also fewer in number, and smaller. Although the specific phases cannot be determined by EDS alone, these are likely dispersoids of the α-AlMn(Fe)Si type, which is commonly found in Al-Mg-Si alloys containing a sufficient amount of Mn [41, 42]. A large amount of such dispersoid particles were also found by TEM, both submerged in the matrix, and on the grain boundaries. Figure 12 demonstrates a high density of dispersoid particles, and their pinning of the grain boundaries.

### 3.7. Precipitate structures

Images of the precipitate structures of the T6 tempers are presented in Figure 13. The precipitate sizes are smaller and denser for alloy A, as compared to the reference alloy. Moreover, the addition of Cu has resulted in precipitates with a rectangular cross-section, which were not found in the reference alloy.

The sizes and density of the precipitates found in alloy B were similar to the ones found in the reference alloy. However, the presence of Cu in alloy C resulted in similar precipitates as were found in alloy A. Yet, the precipitates found in alloy C were considerably smaller and denser than those found in alloy A, and seemingly of different types.

## 4. Discussion

### 4.1. Recrystallized alloys

Due to the low solubility of Fe in the aluminum matrix, the number and sizes of the primary particles are expected to correlate with the Fe content. As seen in Table 3, this is evident for alloy A which contained a higher number density of particles, covering a larger area, than the alloys with only 0.20 wt% Fe. Relating the ratio of wt% $Fe_A$ and $Fe_{Ref}$ (=2.27) with the ratio of the number density of particles in the respective alloys (=2.29), the correspondence is evident. The ratio of the respective area fractions yields a similar result (=2.63), which further suggests a strong correlation. The distribution spread of the particle sizes, however, is more or less of the same order of magnitude for both alloys, and only slightly shifted towards larger particles for alloy A, indicating less influence of the Fe content on particle size. This observation may be due to the breaking up of particles during the extrusion process. However, possible differences in particle sizes as an effect of the Fe content may have been counteracted by differences in the homogenisation procedure. The transformation from coarse β- to smaller α-particles is strongly temperature dependent [17], and since the reference alloy was homogenised at a lower temperature than alloy A, one would perhaps expect to find more β-particles in this alloy. The EDS (Figure 6) and Alstruc results, on the other hand, indicated that the temperature difference might be too low to have a significant effect on the primary particle transformation.

Conventionally, one might expect a decrease in ductility with increasing Fe content. However, in spite of the considerably larger density and area fraction of primary particles, alloy A displayed the highest ductility of the two recrystallized alloys, and a notably larger dimple fraction. The introduction of more Fe, and Cu, seems to have changed the grain boundary characteristics. Similar results have previously been found in an extensive study by Kato et al. [43], who reported an increase in strength and ductility with increasing Fe content in excess Si alloys. In their work, this was partly attributed to the effect of more particle stimulated nucleation (PSN) during recrystallization, with a resulting decrease in grain sizes with increasing Fe content. However, the grain size distribution for alloy A in this work indicated larger grains than for the reference alloy, thus the same explanation is not valid for the improvement in ductility in the present investigation. Instead, it is suggested that it may be due to the interaction between Fe and Si during processing, e.g. in the formation of primary particles, as this would affect the available Mg and Si during solutionizing and ageing.

It is clear from the results in Figure 11 that (Mg,Si) particles have precipitated on the grain boundaries in the reference alloy. The results show a high concentration of Si, and no, or a low concentration, of Mg. Two of the particles analysed are likely pure Si particles, however, the others are most likely $Mg_2Si$. The amount of Mg does not correspond to the $Mg_2Si$ phase, but this is probably due to the strong reaction between $Mg_2Si$ and water, reducing the amount of Mg in the particles during sample preparation [44]. These particles likely have an effect on the grain boundary brittleness. Aucote and Evans [28] concluded that there were two main mechanisms that may account for the brittleness of excess-Si alloys. One was an increasing difference in strength between the grain interior and the grain boundary region due to a finer precipitation structure, and the other a network of Si- and $Mg_2Si$-particles at grain boundaries which are expected to part easily from the matrix to form micro-voids leading to intergranular fracture. The former seems contradictory here, as the presence of Cu in alloy A increased the strength of the matrix, without deteriorating the ductility. However, the latter provides a likely explanation for the early intergranular fracture for the reference alloy.

As these alloys were preheated prior to extrusion, and were water-quenched after, it is most likely that the (Mg,Si) particles have precipitated either during solution or ageing heat

treatment. As the particles were found on the grain boundaries, the recrystallized microstructure further suggests that precipitation must have occurred after extrusion. Closer inspection of the Al-Mg-Si-Fe phase diagram reveals that, for alloy Ref, a solutionizing temperature of 803 K (530 °C) is below the solvus line. This means that some of the grain boundary particles found were likely precipitated during solution heat treatment. Such an occurrence would also decrease the Mg:Si ratio, giving more excess Si in the matrix, and a higher susceptibility for the formation of Si-particles during ageing. Some coarse grain boundary precipitation has therefore most likely also occurred during ageing heat treatment. Similar particles were also found in alloy A, but much fewer. It is thus possible that the increased ductility of alloy A results from both a lower solvus temperature due to the higher solute content, and the removal of Si from solution in the formation of primary particles, leaving less for segregation to grain boundaries during later heat treatment. This fairly low solution temperature was chosen in order to retain the favourable grain structure of these alloys. However, it seems clear that the negative effects related to grain boundary precipitation considerably outweighs the potential positives from controlling the grain structure.

As an increase in excess Si is known to increase the strength, the strength would be expected to decrease with a larger amount of Si tied up in primary particles. In the work by Kato et al. [43], this seemed to have been counteracted by grain boundary strengthening, resulting in an increase in both strength and ductility. However, in the current study, the addition of Fe in alloy D resulted in an increase in ductility, but a decrease in strength. The grain sizes with a higher Fe content were not found to be smaller than for Ref. Rather, possibly due to the differences in homogenisation temperature, they were found to be larger. Thus, the promising results from Kato's [43] work, in terms of increasing *both* strength and ductility by increasing the Fe content, were not successfully reproduced.

The increase in ductility for alloy A in this work is much larger than what was found for alloy D. This suggests that the presence of Cu also has a strong influence on the ductility, which has been reported in previous studies [45-47]. Similar results were found in the study by Kato et al. [43]; however, the mechanism is still unclear. Kato suggested that the presence of Cu could lead to an increasing amount of Si-rich precipitates, which have been found for excess Si alloys in a previous work [46]. This could further reduce the amount of free Si. It was also suggested that it could be due to a better coherency at the interface between the grain boundary precipitates and the Al-matrix. This has not been confirmed, but it is evident that the presence of Cu influences the precipitate structure. The precipitates are both smaller and denser for alloy A, as demonstrated in Figure 13. The large increase in yield strength of alloy A is likely to be attributed to this factor. The effect of Cu on the ageing precipitation of Al-Mg-Si alloys has been thoroughly studied in recent years, and Matsuda et al. [47, 48] found that Cu tends to segregate to the interface of α-Al and metastable phases in an Al-Mg-Si alloy with Cu. This was suggested to reduce the diffusional growth of the precipitates. There are clear indications that the addition of Cu also has introduced different precipitate types in alloy A. The rectangular cross-section of the majority of precipitates in Figure 12b is similar to what has previously been found for the lath-shaped precursory phases of Q', e.g. the so-called L-phase [23, 32]. These phases are known to have a significant effect on the material strength. What effect the different precipitates may have on the ductility is less clear, and other aspects, also influenced by Cu, may be more relevant.

Although Cu has had a positive effect on ductility, the increased strength of the precipitate structure is likely partly responsible for the intergranular fracture. As discussed above, one of the factors responsible for brittleness in excess-Si alloys is an increasing difference in strength between the grain interior and the grain boundary region due to a finer precipitation structure [28]. This principle obviously also holds for Cu-precipitates, and is

10

likely the reason for a weakened grain boundary region. Similarly, the positive contribution of Fe on ductility may also have had a negative effect. Even if the ductility improved with a larger amount of Si in primary particles, the significant amount of primary particles in alloy A is likely the reason for the intergranular fracture observed in Figure 9. Due to the high number density of primary particles in alloy A, more of these are also expected to be present on the grain boundaries in alloy A as compared to the reference alloy. Thus, although adding Fe and Cu has increased ductility by improving grain boundary characteristics, it somewhat ironically also seems to be responsible for the intergranular fracture.

Also an improvement in the elongation to necking was observed for alloy A. Table 4 shows a higher tensile strain for alloy A as compared to the reference alloy. This property commonly improves with the work hardening rate, and alloy A consistently displays a steeper curve until the point of necking in the stress-strain curve in Figure 8. The work hardening rate, calculated through $\theta = d\sigma / d\varepsilon$ and based on the values in Table 4, results in 531 MPa for the reference alloy, and 777 MPa for alloy A. Primary particles are generally not assumed to provide a significant contribution to the work hardening behavior [49], but Cu in solid solution has a sufficient misfit in the aluminum matrix to affect the dislocation mobility [18, 50]. Assuming that the precursory phases to Q and Q' have a similar composition to their stable phases (Q: $Al_4Cu_2Mg_8Si_7$ [31]), and that all precipitates are of this type, an estimation of the amount of Cu in solid solution may be given. The precipitate formation will for alloy A then be controlled by the Mg content, and the solute fraction in precipitates would be 0.89 at% Mg, 0.78 at% Si and 0.22 at% Cu. The resulting amount of Cu in solid solution would be approximately 0.34 - 0.22 = 0.12 at% Cu. Although investigations with e.g. atom probe is the only way to confirm the solid solution level, the calculation should at least not be a large overestimation. It is likely that the Cu-containing alloys contain a certain amount of β'' ($Mg_5Si_6$) precipitates as well [23], which would mean that less Cu is precipitated than what has been estimated above. It is therefore considered a reasonable assumption that the increased work hardening and tensile strain of alloy A comes as a consequence of solid solution hardening.

### 4.2. Fibrous alloys

Alloys B and C both contained a higher area fraction and number density of particles than the reference alloy, which is attributed to the presence of Mn, participating in the formation of primary particles. Mn is also known to ease the transformation from brittle β-AlFeSi to more ductile α-particles, and this has been shown spheroidize the particles, and reduce their average sizes [15, 51]. Figure 5 Figure 5suggests such a relation, as the primary particle size distributions are shifted to the left, and towards smaller particle sizes. Moreover, according to Table 3, the Mn-containing alloys also contain more spherical particles. The average of the min/max Feret diameters yields ~0.45 for alloys B and C, and ~0.33 for A and B. This further suggests more α-particles. These indications were strengthened by the EDS results in Figure 6 Figure 6and simulations by Alstruc, which suggested that only α-particles should be present in the Mn-containing alloys.

Smaller primary particles sizes, and α- instead of β-particles, is likely partly responsible for the improved ductility of these alloys, as compared to alloys Ref and A. However, other factors may also be of significance, e.g. the precipitation of dispersoids. In contrast to the recrystallized alloys, Figure 10 shows a purely transgranular fracture mode for these two alloys. The (Mg,Si) particles found on the grain boundaries in the referance alloy and alloy A were not found here, even though alloy B has a lower Mg:Si ratio than the reference alloy. It is therefore assumed that the precipitation of Mn-dispersoids, in addition to increasing the area fraction of primary particles, has removed a significant amount of Si from

solid solution, leaving less free Si for grain boundary segregation. Moreover, the addition of Mn has lowered the solvus temperature, avoiding precipitation of $Mg_2Si$ during solutionizing.

Small precipitates were also found on the grain boundaries in these alloys, but containing Mn and Si. They were fewer and smaller in sizes than the Mg/Si-particles found in the recrystallized alloys, and are likely dispersoids of type α-Al(MnFe)Si. TEM micrographs in Figure 12Figure 12 reveal a high density of such small dispersoids precipitated during homogenisation, which in addition to removing Si from solution contributed to retaining the deformation substructure after extrusion. A subgrain structure gives a contribution to the strength through a Hall-Petch effect, and the dispersoids work as obstacles for dislocation movement, increasing the work hardening. Thus, despite a ~0.1 wt% lower Mg content, the strength of alloy B is increased as compared to Ref. Moreover, earlier findings have suggested that dispersoids may give a direct contribution to the ductility. Nam and Lee [52] and Lee et al. [53] have suggested that Mn-dispersoids also provoke a change in the slip behavior of dislocations, promoting cross-slip, which leads to more uniform deformation and thus improving ductility. In addition to the above mentioned aspects, in the event of grain boundary precipitation, the precipitation is likely to be more evenly distributed in alloys with a substructure, due to the larger grain boundary area. A subgrain structure should thus reduce the risk of coarse grain boundary precipitation.

The lowest uniform tensile strain was observed for alloy B, and is presumably due to its relatively poor work hardening. Its lower work hardening, as compared to the reference alloy, is expected to be due to the fibrous structure, as those have previously been found to reduce the work hardening and tensile strain of aluminum alloys [54]. This is also seen for alloy C, which despite having the largest work hardening still had a lower tensile strain than alloy A, and the same elongation to necking as the reference alloy.

As Cu is a major strengthening element in Al-Mg-Si alloys, the strength would be expected to increase with increasing Cu content. This is not found to be the case, as alloy C displays a higher yield strength than alloy A. As for alloy A, the addition of Cu significantly changed the precipitate structure of alloy C, as compared to alloys Ref and B. The precipitate sizes are smaller and the density higher. However, alloy C also has a higher precipitate density than alloy A. This, in addition to the retained substructure, is likely the reason for its improved yield strength as compared to alloy A. Smaller sizes and a higher density is probably due to a combined effect of a lower availability of Si and Cu, and the effect of Cu to decrease the diffusional growth of the precipitates [47, 48]. However, alloy C also displays the highest work hardening rate of the alloys, which suggests solid solution strengthening. The solid solution level of Cu in alloy C may be estimated by using the same approach as with alloy A. For this alloy, however, due to the high Mg content, the precipitation would be limited by the available Si. The solute fraction in Q or Q' precursor precipitates for alloy C would be 0.43 at% Mg, 0.38 at% Si and 0.11 at% Cu, resulting in 0.17 - 0.11 = 0.06 at% Cu. These same calculations reveal the estimated amount of Mg in solid solution, which is quite large at 1.13 − 0.43 = 0.7 at% Mg. Alstruc also indicated a certain amount of Mn in solid solution, however, Mg is clearly the main contributor to the large work hardening for alloy C.

The increase in yield strength due to the precipitates have also contributed to a decrease in ductility for alloy C, as compared to alloy B. However, in this case it has not lead to intergranular fracture, and may not be explained by the same factors as when comparing the recrystallized alloys. A possible explanation arises from classical theory on void formation during tension, where a void will form when a critical normal stress for decohesion of particle/matrix or cracking of a particle is reached. Between alloys B and C, it is therefore likely that the high stress levels of alloy C result in a lower strain at which void nucleation initiates. The initial work hardening of alloy C is large, and the matrix is more likely to resist void growth at this stage. However, after necking this is no longer the case, and the work

hardening of the two fibrous alloys proceeds at a similar rate. Consequently, as a larger amount of primary particles were found in alloy C, these voids would be expected to link up more easily at increasingly higher strains. However, a difference in the average particle sizes between these two alloys was found, and it seems reasonable to assume that the lower Si content in alloy C is responsible for the smaller particle sizes as compared to alloy B. This is likely to have been favourable for the ductility of alloy C, although less than other factors.

## 5. Conclusions

The current study has documented the combined effect of different alloying elements (i.e. Fe, Cu and Mn) on the microstructure and associated stress-strain behavior of extruded Al-Mg-Si alloys. A particular emphasis has been placed on the ductility to fracture behavior monitored by a laser-extensometer and by explicit analysis of the fracture surfaces. These studies have provided new insight into the strength/ductility behavior of such alloys, and several new and interesting results were found.

Although traditionally seen as detrimental to mechanical properties, Fe and primary particles were not found to have a negative effect on ductility, but rather a slightly positive effect. Instead, other factors were found more dominant in reducing the elongation to fracture. The reference alloy showed poor ductility due to the presence of (Mg,Si) particles on the grain boundaries, some of which precipitated prior to ageing. Although this alloy was not very high in excess Si, it must be pointed out that the precipitation of $Mg_2Si$ particles prior to ageing, either during homogenisation/extrusion or solutionizing, lowers the Mg:Si ratio, and increases the likelihood of pure Si precipitation during ageing. Moreover, such $Mg_2Si$ particles will themselves reduce ductility. The benefit of Fe is thus found to come as an effect of reducing the precipitation potential of coarse (Mg,Si) phases, due to the formation of primary particles.

The present study has not been successful in clarifying all the mechanisms responsible for the influence of Cu on the relevant Al-Mg-Si alloys. Nevertheless, the results for the Cu-containing alloys A and C support previous reports that Cu influences ductility in a positive way, where the likely presence of a significant amount of Cu in solid solution explains the improvement in tensile strain for these alloys. The influence of Cu on ductility is seen as an important topic by the authors, and a deeper understanding of its mechanisms is necessary to further improve Cu-containing Al-Mg-Si alloys.

Mn had the most positive effect on ductility. In addition to the precipitation of dispersoids preventing recrystallization, the introduction of Mn also reduced the average size of the primary particles, by transformation of β-AlFeSi to α-phase particles. This effect is likely to have improved the ductility, resulting in less brittle particles in the structure. Factors related to the precipitation of dispersoids were found to be positive for ductility, but although a fibrous structure enhances ductility, it seems to have a negative effect on tensile strain.

Finally, excess-Si is often added to increase the precipitation rate during ageing, in applications where rapid ageing and high strength is more important than ductility. The results for alloy C, however, suggests that by increasing the Mg:Si ratio, the ductility will be improved for the same (or lower) total content of Mg+Si, while the precipitation kinetics and strength may be retained by adding back Cu.

## 6. Acknowledgements

## 7. References

1. D. J. Chakrabarti and D. E. Laughlin, *Prog. Mater. Sci.,* 2004, vol. 49, pp. 389-410.
2. R. D. Doherty, D. A. Hughes, F. J. Humphreys, J. J. Jonas, D. J. Jensen, M. E. Kassner, W. E. King, T. R. McNelley, H. J. McQueen and A. D. Rollett, *Mater. Sci. Eng., A,* 1997, vol. 238, pp. 219-274.
3. P. Haasen, in *Physical Metallurgy (Fourth Edition),* (North-Holland: Oxford, 1996), pp. 2009-2073.
4. Ø. Ryen, B. Holmedal, O. Nijs, E. Nes, E. Sjölander and H. E. Ekström, *Metall. Mater. Trans. A,* 2006, vol. 37, pp. 1999-2006.
5. Q. Zhao, M. Slagsvold and B. Holmedal, *Scr. Mater.,* 2012, vol. 67, pp. 217-220.
6. D. J. Lloyd, *Scr. Mater.,* 2003, vol. 48, pp. 341-344.
7. R. Z. Valiev, I. V. Alexandrov, Y. T. Zhu and T. C. Lowe, *J. Mater. Res.,* 2002, vol. 17, pp. 5-8.
8. J. D. Embury, W. J. Poole and D. J. Lloyd, *Mater. Sci. Forum,* 2006, vol. 519, pp. 71-78.
9. A. K. Ghosh, *J. Eng. Mater. Technol.,* 1977, vol. 99, pp. 264-274.
10. J. W. Hutchinson and K. W. Neale, *Acta Metall.,* 1977, vol. 25, pp. 839-846.
11. S. H. Goods and L. M. Brown, *Acta Metall.,* 1979, vol. 27, pp. 1-15.
12. F. A. McClintock, *J. Appl. Mech.,* 1968, vol. 35, pp. 363-371.
13. I. Westermann, K.O. Pedersen, T. Furu, T. Børvik and O.S. Hopperstad, *Mech. Mater.,* 2014, vol. 79, pp. 58-72.
14. G. Sha, K.A.Q. O'Reilly and B. Cantor, in *Mater. Sci. Forum,* (2006), pp. 1721-1726.
15. K. B. S. Couto, S. R. Claves, W. H. Van Geertruyden, W. Z. Misiolek and M. Goncalves, *Mater. Sci. Technol.,* 2005, vol. 21, pp. 263-268.
16. S. Zajac, B. Hutchinson, A. Johansson and L. O. Gullman, *Mater. Sci. Technol.,* 1994, vol. 10, pp. 323-333.
17. S. Onurlu and A. Tekin, *J. Mater. Sci.,* 1994, vol. 29, pp. 1652-1655.
18. T. Sheppard: *Extrusion of aluminium alloys.* (Springer Science & Business Media, 1999).
19. G. Mrówka-Nowotnik, J. Sieniawski and M. Wierzbiñska, *Arch. Mater. Sci. Eng.,* 2007, vol. 28, pp. 69-76.
20. N. C. W. Kuijpers, F. J. Vermolen, C. Vuik, P. T. G. Koenis, K. E. Nilsen and S. van der Zwaag, *Mater. Sci. Eng., A,* 2005, vol. 394, pp. 9-19.
21. F. J. Humphreys and G. W. Lorimer, in *Advanced Light Alloys and Composites*, ed. R. Ciach (Springer Netherlands: 1998), pp. 343-353.
22. L. M. Cheng, W. J. Poole, J. D. Embury and D. J. Lloyd, *Metall. Mater. Trans. A,* 2003, vol. 34, pp. 2473-2481.
23. C.D. Marioara, S.J. Andersen, T.N. Stene, H. Hasting, J. Walmsley, A.T.J. Van Helvoort and R. Holmestad, *Philos. Mag.,* 2007, vol. 87, pp. 3385-3413.
24. S. J. Andersen, H. W. Zandbergen, J. Jansen, C. Træholt, U. Tundal and O. Reiso, *Acta Mater.,* 1998, vol. 46, pp. 3283-3298.
25. A. K. Gupta, D. J. Lloyd and S. A. Court, *Mater. Sci. Eng., A,* 2001, vol. 336, pp. 11-17.
26. M Murayama and K Hono, *Acta materialia,* 1999, vol. 47, pp. 1537-1548.
27. N. Maruyama, R. Uemori, N. Hashimoto, M. Saga and M. Kikuchi, *Scr. Mater.,* 1997, vol. 36, pp. 89-93.
28. J. Aucote and D. W. Evans, *Mater. Sci. Technol.,* 1978, vol. 12, pp. 57-63.
29. S. M. Hirth, G. J. Marshall, S. A. Court and D. J. Lloyd, *Mater. Sci. Eng., A,* 2001, vol. 319–321, pp. 452-456.

30. Y. Kato, K. Hisayuki, M. Sakaguchi and K. Higashi, *Int. Conf. Alum. Alloys, 13th,* 2012, pp. 1521-1526.
31. L. Arnberg and B. Aurivillius, *Acta Chem. Scand. A,* 1980, vol. 34, p. 1.
32. D.J. Chakrabarti, Y. Peng and D.E. Laughlin, in *Mater. Sci. Forum,* (2002), pp. 857-862.
33. C. D. Marioara, S. J. Andersen, J. Røyset, O. Reiso, S. Gulbrandsen-Dahl, T. E. Nicolaisen, I. E. Opheim, J. F. Helgaker and R. Holmestad, *Met. Mat. Trans. A,* 2014, vol. 45, pp. 2938-2949.
34. W. S. Rasband, C. A. Schneider and K. W. Eliceiri, *Nat. Methods,* 2012, vol. 9, p. 671.
35. P.W. Bridgman, *Trans. Am. Soc. Met.,* 1944, vol. 32, p. 553.
36. G. E. Dieter: *Mechanical Metallurgy*. 3rd ed. (McGraw-Hill, 1988), pp. 292-293.
37. G. Le Roy, J.D. Embury, G. Edward and M.F. Ashby, *Acta Metall.,* 1981, vol. 29, pp. 1509-1522.
38. M. Qian, J. A. Taylor, J. Y. Yao, M. J. Couper and D. H. StJohn, *Journal of Light Metals,* 2001, vol. 1, pp. 187-193.
39. A. L. Dons, *J. L. Met.,* 2001, vol. 1, pp. 133-149.
40. A. L. Dons, E. K. Jensen, Y. Langsrud, E. Trømborg and S. Brusethaug, *Metall. Mat. Trans. A,* 1999, vol. 30, pp. 2135-2146.
41. L. Lodgaard and N. Ryum, *Mater. Sci. Eng., A,* 2000, vol. 283, pp. 144-152.
42. K. Strobel, E. Sweet, M. Easton, J. F. Nie and M. Couper, *Mater. Sci. Forum,* 2010, vol. 654-656, pp. 926-929.
43. Y. Kato, K. Hisayuki, M Sakaguchi and K. Higashi, in *Int. Conf. Alum. Alloys, 13th,* (2012), pp. 1521-1526.
44. E. Linardi, R. Haddad and L. Lanzani, *Proc. Mater. Sci.,* 2012, vol. 1, pp. 550-557.
45. S. Ikeno, K. Matsuda, K Nakajima, S. Rengakuji and Y. Uetani, *J. Jpn. Inst. Light Met.,* 1998, vol. 48, pp. 207-211.
46. K. Matsuda, S. Ikeno, Y. Uetani and T. Sato, *Metall. Mater. Trans. A,* 2001, vol. 32, pp. 1293-1299.
47. K. Matsuda, D. Teguri, T. Sato, Y. Uetani and S. Ikeno, *Mater. Trans.,* 2007, vol. 48, pp. 967-974.
48. K. Matsuda, D. Teguri, Y. Uetani, T. Sato and S. Ikeno, *Scr. Mater.,* 2002, vol. 47, pp. 833-837.
49. A. Kelly and R. B. Nicholson: *Strengthening methods in crystals*. (Elsevier, 1971).
50. G. P. M. Leyson, W. A. Curtin, L. G. Hector and C. F. Woodward, *Nat. Mater.,* 2010, vol. 9, pp. 750-755.
51. S. R. Claves, D. L. Elias and W. Z. Misiolek, *Mater. Sci. Forum,* 2002, vol. 396, pp. 667-674.
52. S. W. Nam and D. H. Lee, *Met. Mater. Int.,* 2000, vol. 6, pp. 13-16.
53. D. H. Lee, J. H. Park and S. W. Nam, *Mater. Sci. Technol.,* 1999, vol. 15, pp. 450-455.
54. K. O. Pedersen, O. G. Lademo, T. Berstad, T. Furu and O. S. Hopperstad, *J. Mater. Process. Technol.,* 2008, vol. 200, pp. 77-93.

**Table 1: The chemical composition of the alloys investigated in this study, given in wt%. Mg:Si is the atomic ratio of Mg and Si.**

| Alloy | Si | Fe | Cu | Mg | Mn | Mg:Si |
|-------|------|------|------|------|------|-------|
| Ref | 0.95 | 0.22 | - | 0.75 | - | 0.91 |
| A | 1.00 | 0.50 | 0.80 | 0.80 | - | 0.92 |
| B | 1.00 | 0.20 | - | 0.66 | 0.55 | 0.76 |
| C | 0.52 | 0.21 | 0.40 | 1.01 | 0.55 | 2.24 |
| D | 1.00 | 0.50 | - | 0.80 | - | 0.92 |

**Table 2: The settings used for the different SEM investigations.**

| Setting | Particle analysis | Chemical analysis (Primary particles) | Chemical analysis (GB particles) | Grain sizes | Fractography |
|---------|-------------------|---------------------------------------|----------------------------------|-------------|--------------|
| Operation mode | BSE | EDS | EDS | EBSD | SE |
| Acceleration voltage | 15 kV | 20 kV | 4 kV | 20 kV | 20 kV |
| Working distance | 15 mm | 12.5 mm | 10 mm | ca 23 mm | 10-30 mm |
| Current mode | High current | High current | High Current | High current | High current |
| Aperture diameter | 60 μm | 120 μm | 60 μm | 300 μm | 30 μm |
| Tilting angle | 0° | 0° | 0° | 70° | 0° |

**Table 3: Results from the primary particle analysis. The error indicates the standard deviation between the three images analysed for each alloy.**

| | Ref | A | B | C |
|-------|-----|---|---|---|
| **Count** | 519 ± 19 | 1192 ± 25 | 712 ± 31 | 849 ± 94 |
| **ECD [μm]** | 1.65 ± 0.06 | 1.76 ± 0.03 | 1.59 ± 0.02 | 1.31 ± 0.06 |
| **%Area** | 0.80 ± 0.08 | 2.09 ± 0.06 | 1.02 ± 0.05 | 0.84 ± 0.16 |
| **min/max Feret** | 0.31 ± 0.01 | 0.33 ± 0.00 | 0.46 ± 0.01 | 0.43 ± 0.00 |

**Table 4: Important values from the tensile tests.**

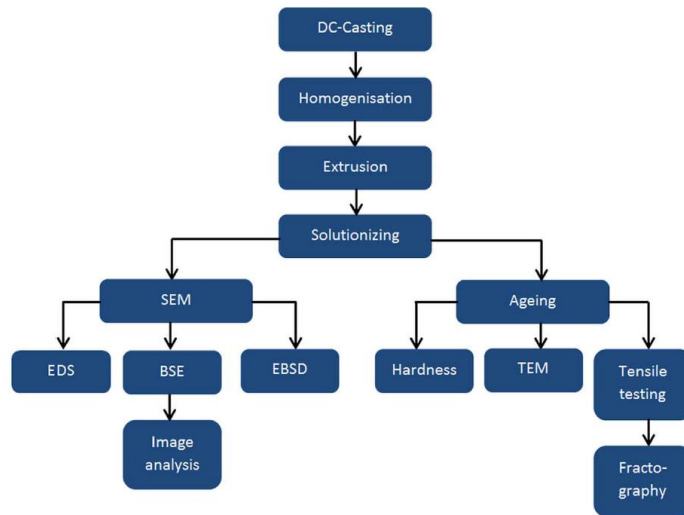| Alloy | Yield strength $\sigma_{0.2}$ [MPa] | Tensile strength $\sigma_{UTS}$ [MPa] | Tensile strain $\varepsilon_{UTS}$ [mm/mm] | Fracture strain $\varepsilon_{frac}$ [mm/mm] |
|-------|------------------|-------------------|----------------|----------------|
| Ref | 308 ± 1 | 358 ± 0 | 0.095 ± 0.001 | 0.230 ± 0.008 |
| A | 347 ± 0 | 434 ± 2 | 0.111 ± 0.002 | 0.439 ± 0.017 |
| B | 353 ± 1 | 388 ± 2 | 0.072 ± 0.001 | 0.774 ± 0.019 |
| C | 376 ± 1 | 454 ± 3 | 0.091 ± 0.004 | 0.649 ± 0.002 |
| D | 290 ± 1 | 345 ± 0 | 0.087 ± 0.001 | 0.279 ± 0.007 |

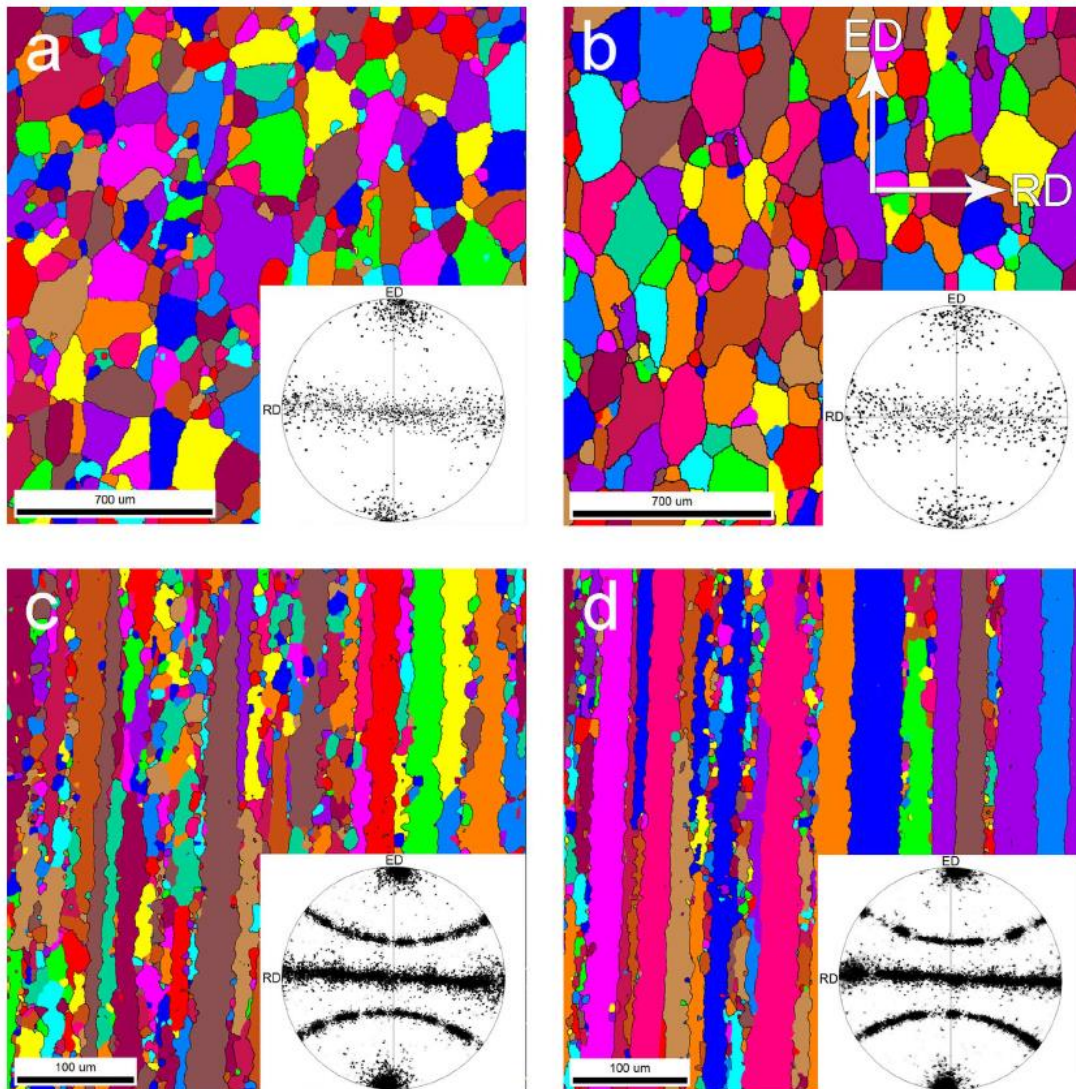**Figure 1: A flow chart of the experimental procedure.**



**Figure 2: EBSD maps of the extrudates revealing a recrystallized grain structure for Ref (a) and A (b), and a mixed grain structure for B (c) and C (d). Due to the difference in grain structure two different magnifications were used.**
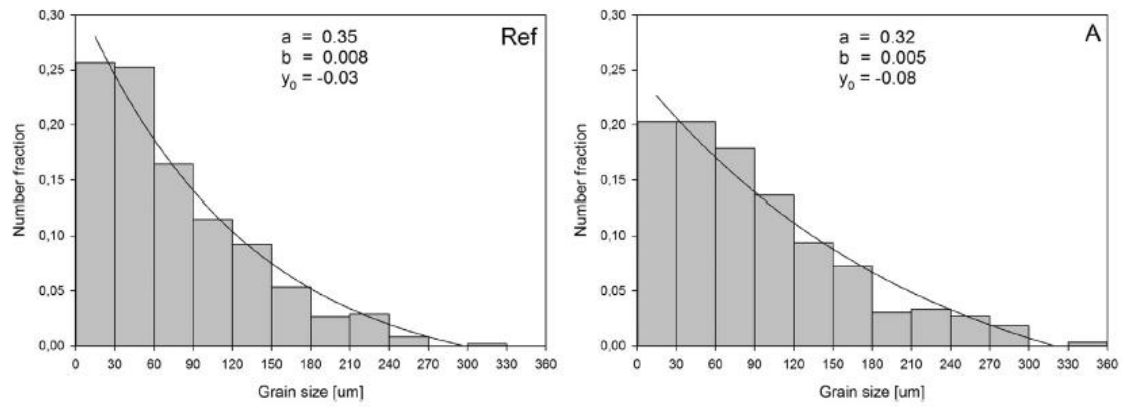
**Figure 3: The grain size distribution of the recrystallized alloys. The distribution fitting is exponential decline:**
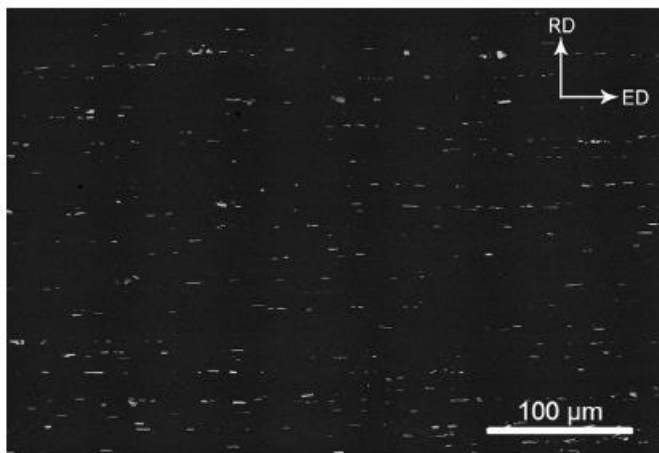$$f = y_0 + a\exp(-bx).$$



**Figure 4: An example of the SEM images analysed, taken from the reference alloy. The primary particles are aligned along stringers in the extrusion direction.**
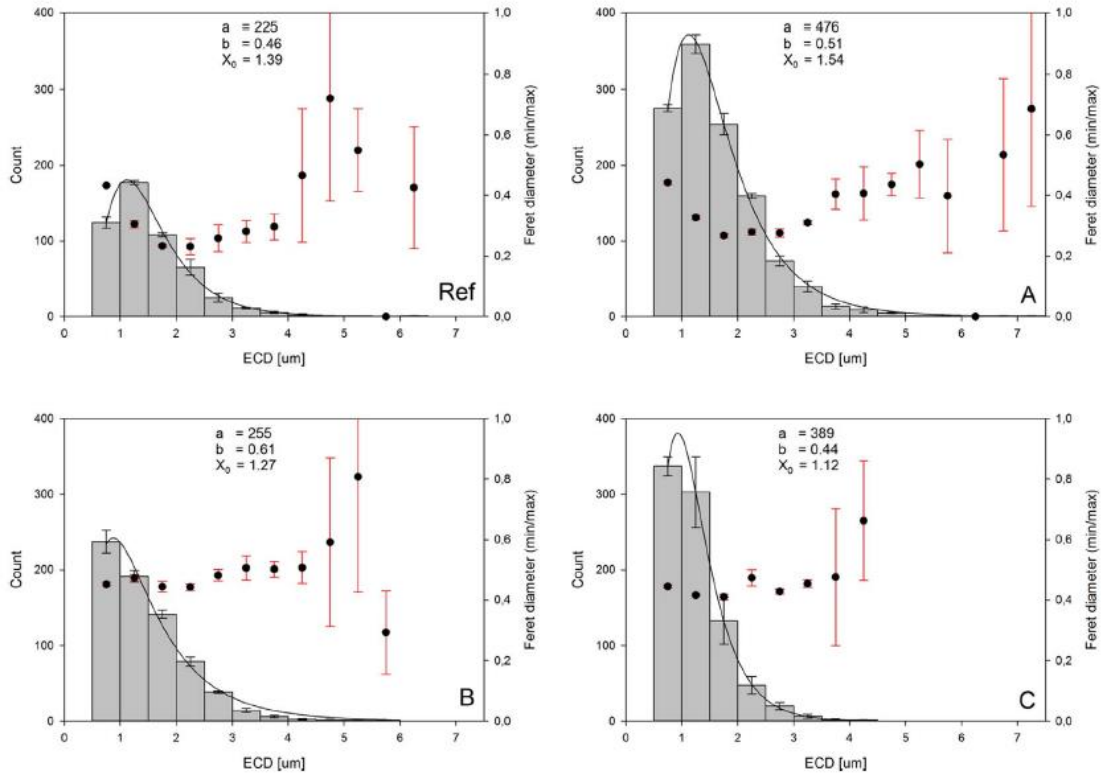
**Figure 5: Particle distribution charts. Grey bars indicate the number of particles in each size interval, while black dots indicate the corresponding average feret diameter. The distribution fitting is log normal:** $f = aexp(-0.5(ln(x/X_0)/b)^2)/2.$
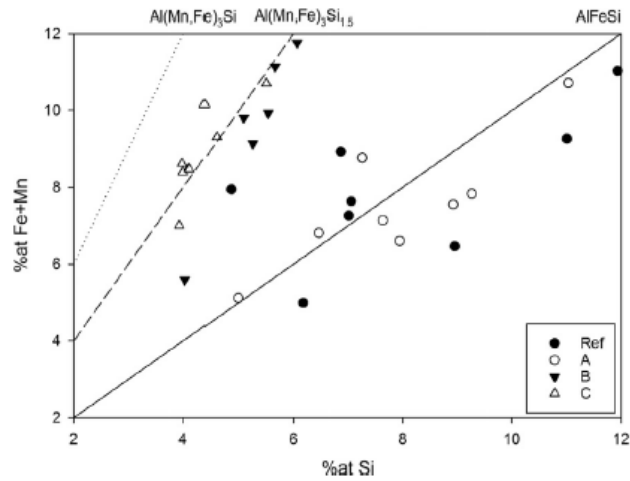


**Figure 6: Result from the EDS analysis. The primary particles in Ref and A seem to align along the β-AlFeSi-line, while the particles in the two Mn-containing alloys, B and C, align along α-Al(Fe,Mn)$_3$Si$_{1.5}$.**
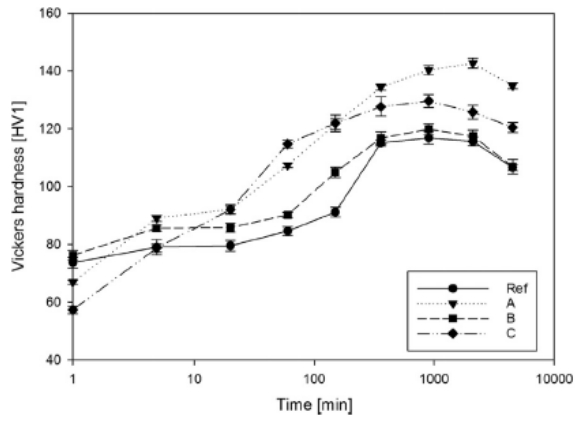
**Figure 7: The ageing behavior of the different alloys.**
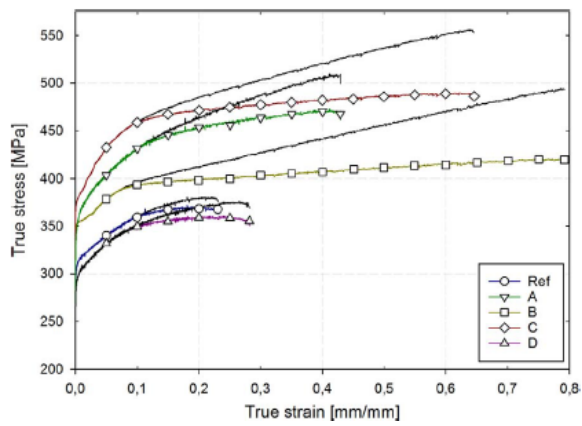


**Figure 8: Stress-strain curves in temper T6, calculated with Bridgman correction. The black curves represent each alloy's non-corrected curve, indicating the initiation of necking at the point in which they separate.**
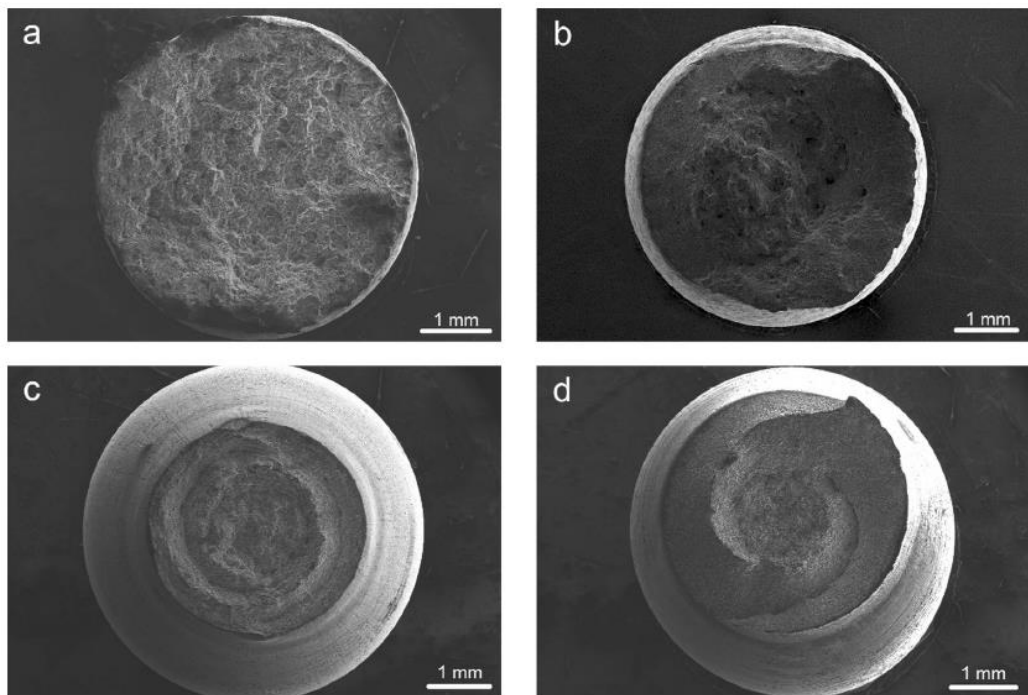


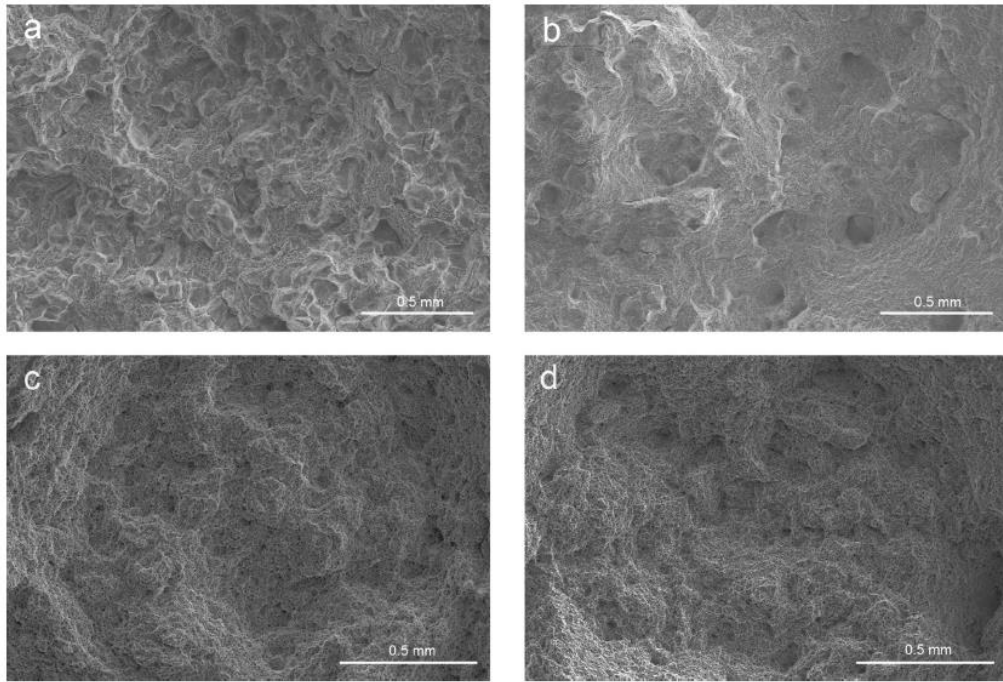**Figure 9: Fracture surfaces of the reference alloy (a), alloy A (b), alloy B (c) and alloy C (d).**

**Figure 10: SEM images of the fracture surfaces, showing intergranular fracture in Ref (a) and A (b), and completely ductile fracture surfaces for B (c) and C (d).**
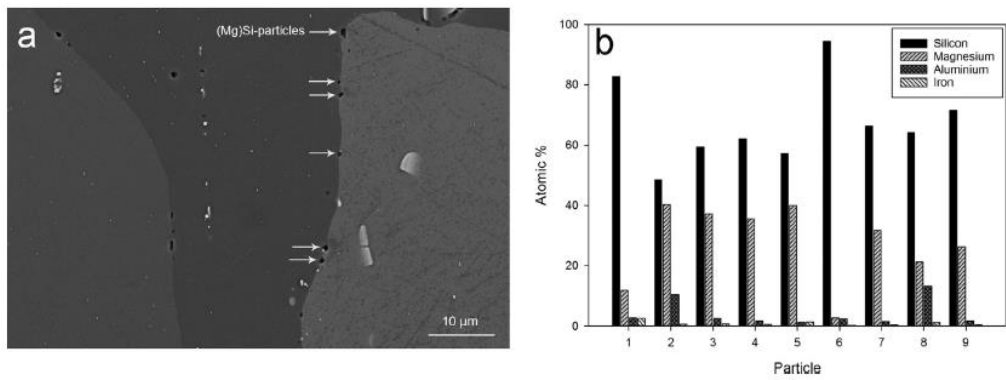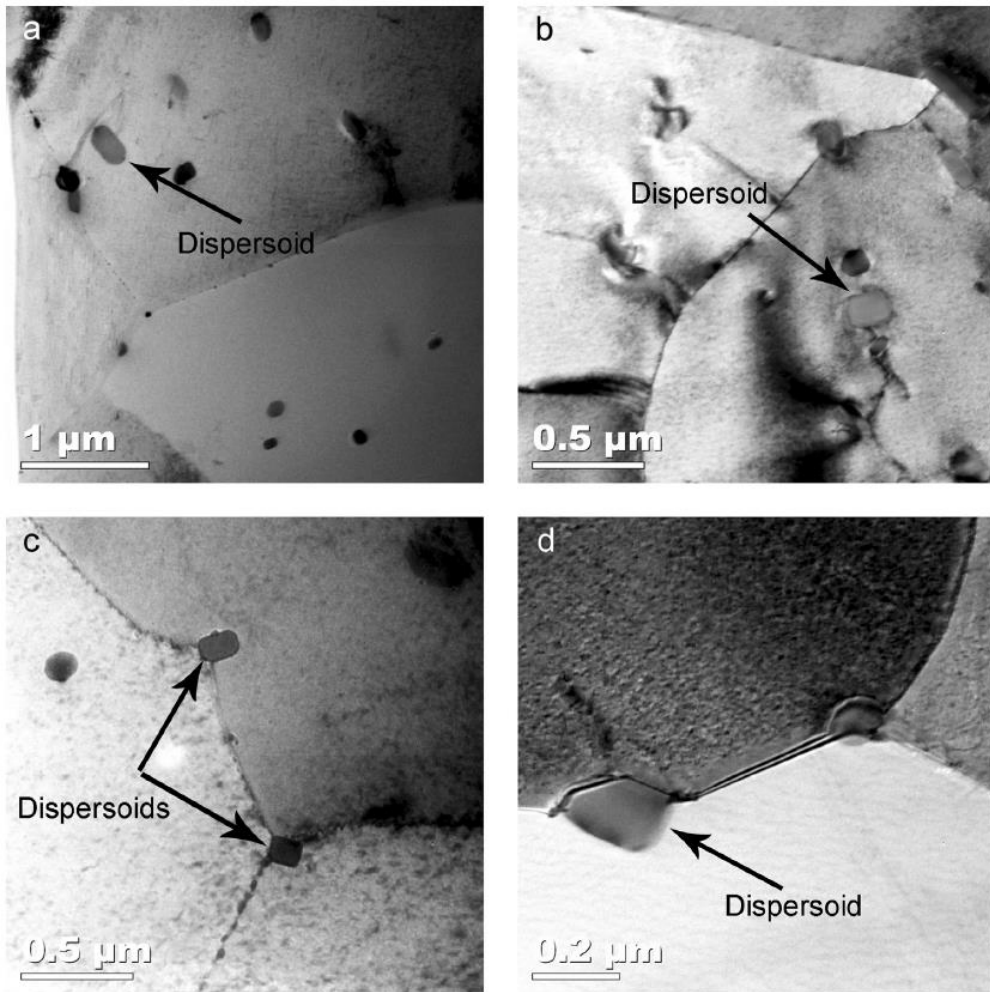


**Figure 11: a) Particles found on grain boundaries in the reference alloy are indicated by white arrows. b) Chemical analysis of dark particles on grain boundaries in the reference alloy.**

**Figure 12: TEM micrographs of dispersoids in the Mn-containing alloys. a) and b) display a high density of dispersoids in alloys B and C, respectively. c) and d) show the pinning of grain boundaries by dispersoids in the same alloys.**
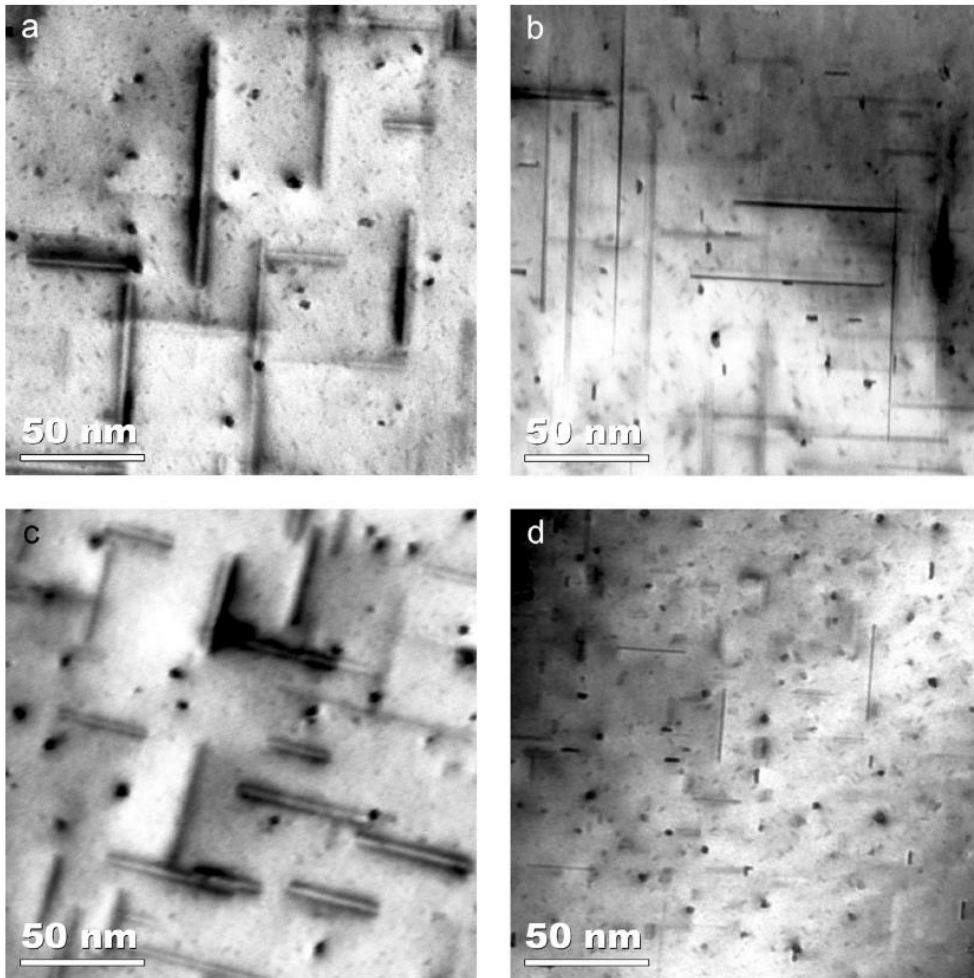
**Figure 13: Precipitate distribution and sizes imaged at 100kX magnification. The precipitate sizes are coarser for Ref (a) and B (c), while the introduction of Cu has resulted in a fine precipitate structure in A (b) and C (d). All images are taken with the matrix oriented in a <100> zone axis.**